# Anisotropic material properties of pure copper with fine-grained microstructure fabricated by laser powder bed fusion process

Shuo Qu [a], Junhao Ding [a], Jin Fu [b], Mingwang Fu [b], Xu Song [a,*]

[a] Department of Mechanical and Automation Engineering, Chinese University of Hong Kong, Shatin, HKSAR, China
[b] Department of Mechanical Engineering, The Hong Kong Polytechnic University, Hung Hom, Kowloon, HKSAR, China

## Abstract

With excellent thermal and electrical conductivity, pure copper has been widely used in many industries. The development of additive manufacturing (AM) enables the prototyping of copper components rapidly and cost-effectively. Especially, Laser powder bed fusion (LPBF), one of the AM techniques, now can fabricate pure copper components with complex geometries. However, the high reflection of laser energy in pure copper at the wavelength used in most commercial fiber laser AM machines posts a challenge in industry practice. To circumvent this problem, higher laser power, different laser wavelength or different energy source (such as electron) have to be adopted, which alleviates the problem of low laser energy absorptivity, but leads to the undesirable tradeoff between the mechanical properties and thermal/electrical performance. In the current study, the high-precision LPBF (HP-LPBF) combining fine beam and small layer thickness managed to achieve the enhanced strength and ductility, while keeping the thermal and electrical conductivity close to the annealed one without heat treatment. Utilizing small layer thickness with scan strategy of 67° rotation angle, the columnar grain growth was inhibited, which weaken the anisotropy of material properties. As a result, pure copper by HP-LPBF outperform those by conventional PBF in mechanical, thermal, and electrical properties with reduce anisotropy.

**Keywords:** High-precision Laser Powder Bed Fusion (HP-LPBF); Anisotropy; Mechanical Properties; Thermal and Electrical Conductivity; Pure Copper

## 1. Introduction

With the fast-paced development in the electronics and electric vehicle industries, pure copper is in great demand due to its high thermal conductivity and electrical conductivity (TC and EC, respectively) [1]. Additive manufacturing (AM), or three-dimensional (3D) printing, has become a breakthrough technology for fabricating complex Cu components, especially for applications that require high TC and EC, such as electromagnetic coils [2, 3], heat exchangers [4, 5], and heat sinks [6, 7]. As the demand for multi-functional AMed components is increasing [8], it is critical to develop an AM method to achieve multi-functional Cu components with good thermal/electrical and mechanical properties.

However, the mechanical properties of pure Cu are usually unsatisfactory for load-bearing applications. Therefore, pure Cu is often replaced by Cu alloys with better mechanical performance to meet the strength requirement, but such alloys usually have lower TC and EC. Thus, in the 3D printing of pure Cu components, it is important to achieve high strength and high ductility, while maintain high TC and EC at the same time.

Powder bed fusion (PBF) technology is an AM technique that enables printing complex and multiscale structures [9]. In particular, the electron beam PBF (EB-PBF) process generates high relative density (RD) in pure Cu components without the issue of low absorption of beam energy [10]. However, EB-PBF often results in high surface roughness and has a limited printing resolution (typically >500 μm) [11-13]. In addition, the relatively low cooling rate and in-situ annealing in the EB-PBF

process often generate large columnar grains, resulting in low yield stress (YS, ~70 MPa) [14].

In contrast, LPBF has inherent advantages over EB-PBF for printing components with intricate features (high resolution) and complicated structures [15], as the former uses finer powders (<53 μm) and smaller beam size than the latter. The conventional LPBF (cLPBF) process typically uses a beam size of 50–200 μm, a layer thickness of 20–50 μm, and a powder size of 15–53 μm [16-19]. However, it is difficult to use this configuration to fabricate pure Cu components with good comprehensive (mechanical, thermal, electrical) performance, due to the high TC and infrared laser reflectivity of pure Cu [20]. Moreover, cLPBF-fabricated components usually contain lack-of-fusion defects with a low RD under 99%[3, 17, 21], resulting in low TC and EC of the components.

Increasing the energy input can achieve high density and reasonable EC and TC, but this high energy density also induces larger molten pools (~400 μm) [19], which negatively affect printing resolution [22]. Recently, short-wavelength LPBF (swLPBF) has been developed for printing pure Cu [23, 24], as the high absorption of short-wavelength laser energy by pure Cu can lead to pore-free microstructure, and their TCs / ECs are among the highest reported. However, swLPBF has a low printing resolution (~500 μm), and its need for expensive laser optics further limits its wide adoption [16, 25].

In the current study, a high-precision LPBF (HP-LPBF) system [7, 26, 27] was

employed to fabricate pure Cu samples. The system uses a 25 μm laser beam, a layer thickness of 10 μm, and a powder size of 5–30 μm. Crucially, in HP-LPBF, a decrease in the beam size increases the concentration of the laser energy, which decreases the laser power required to maintain a given level of volume energy density [19]; a decrease in the layer thickness increases the efficiency of the remelting process between the layers; and a decrease in the size of the powders increases their absorption of laser energy [28]. By combining these three features, HP-LPBF enables the fabrication of pure Cu samples with high resolution, low roughness, and high density simultaneously [26]. Moreover, HP-LPBF tends to yield finer grains than cLPBF [27], and fine-grain microstructure is beneficial for Cu samples, as pulsed electrodeposited pure Cu samples have demonstrated both high strength and high conductivity due to fine grain strengthening [29]. Therefore, HP-LPBF should be employed to create as-printed fine-grained microstructure for pure Cu samples to achieve high comprehensive performance.

LPBFed components often exhibit grain orientation-dependent properties, and the grain orientation of a component is closely related its building direction (BD). In the consecutive layer-by-layer LPBF fabrication process, the thermal gradient direction is approximately aligned with the BD, which inevitably results in a textured microstructure and hence anisotropic material properties. This phenomenon complicates the AM design process, as material anisotropy must be considered at the design stage. Many studies have examined the anisotropic microstructures and properties of LPBFed metallic components [27, 30, 31]. Thomas et al. [14] studied the

4

anisotropy of EB-PBFed pure Cu components, and found that their electrical properties, YS, and ductility were almost isotropic, whereas their work-hardening behaviour was dependent on their texture and thus their BD, as the in-situ annealing in the EB-PBF process led to significant grain growth. Based on studies of other metallic materials [27, 30, 31], the anisotropy of pure Cu components can be attributed to their long columnar grains arising from epitaxial growth. Moreover, although components containing large grains that have few grain boundaries (GBs) may have lower anisotropy than components with small grains that have many GBs, the former are weaker in strength than the latter. Therefore, pure Cu components must be fabricated by a process that involves in-situ grain refinement and inhibits the formation of long and thin columnar grains.

In this work, as-printed pure Cu samples with good comprehensive performance (YS > 200 MPa, elongation of ~40%, TC ~383 W/m·K, EC of ~96% of the International Annealed Cu Standard (IACS)) were fabricated by HP-LPBF. A rotating scan strategy with angle 67° enabled the printed samples to have fine grains and twisted GBs, and thus low anisotropy. These ensured that HP-LPBF-fabricated pure Cu components have better mechanical, thermal, and electrical performance than their conventional PBFed counterparts. Such HP-LPBF approach can be readily extended to additive manufacturing of other reflective metals for many novel and promising applications.

## 2.  Material and methods

### 2.1 Material and process

Detailed configurations of the HP-LPBF machine (Han's Laser M100μ) were given in the previous work [26]. The substrate material is stainless steel 316L. The beam size was 25 μm, and the layer thickness was 10 μm. The difference of process configuration in this work is that the substrate was preheated to 100°C, which improved the wettability of the molten pool and the energy absorption of the powders [32]. In addition, the higher temperature of substrate could reduce the requirement of laser energy and the residual stresses avoiding the formation of microcracks [33]. The process parameters were optimised by evaluating the density and material properties as in previous work [26], and the values were as follows: laser power = 220 W, scan speed = 600 mm/s, and hatch distance = 0.05 mm. Pure copper powders are provided by Jiu Chun New Material Technology (Suzhou) Co., Ltd. The powders ranged in size from 5 to 30 μm, as observed by scanning electron microscopy (SEM) (Fig. 1a); the size distribution is illustrated in Fig. 1b, and their $D_{50}$ was 14.00 μm. Fig. 2a shows the as-printed samples with different testing orientations (0°, 45°, and 90°). Fig. 2b presents the testing sample layout and indicates the scan direction (SD) and the BD; the sample size details are shown in Fig. 2c. Bars of dimension $2 \times 2 \times 30$ mm$^3$ were used in the EC test, and disk-shaped cylinders of diameter 12.7 mm and thickness 2.5 mm were used for the TC test. Cubes of dimension $10 \times 10 \times 10$ mm$^3$ were used to characterise the as-printed morphology by optical microscopy (OM) and electron backscatter diffraction (EBSD). Dog-bone samples of gauge dimension 15 ×

$4 \times 1.5$ mm$^3$ were machined by wire-electrode cutting. Fig. 3 illustrates the relationship between layers at rotating angles of 0° and 67°; each layer was covered by the laser tracks in a zig-zag pattern, where 0° was parallel to the SD. The sample parameters for the scan strategy and BD are listed in Table. 2, and were used to examine the influence of grain morphology on the samples' mechanical performance. The sample process parameters – an as-printed group (AP), a high-power group (HP), and a high-speed group (HS) – and their different linear energy densities $E_l$ were listed in Table. 2 which were used to examine the influence of grain size on the samples' mechanical performance. $E_l$ is calculated as $P/V$, where $P$ is laser power and $V$ is scan speed.
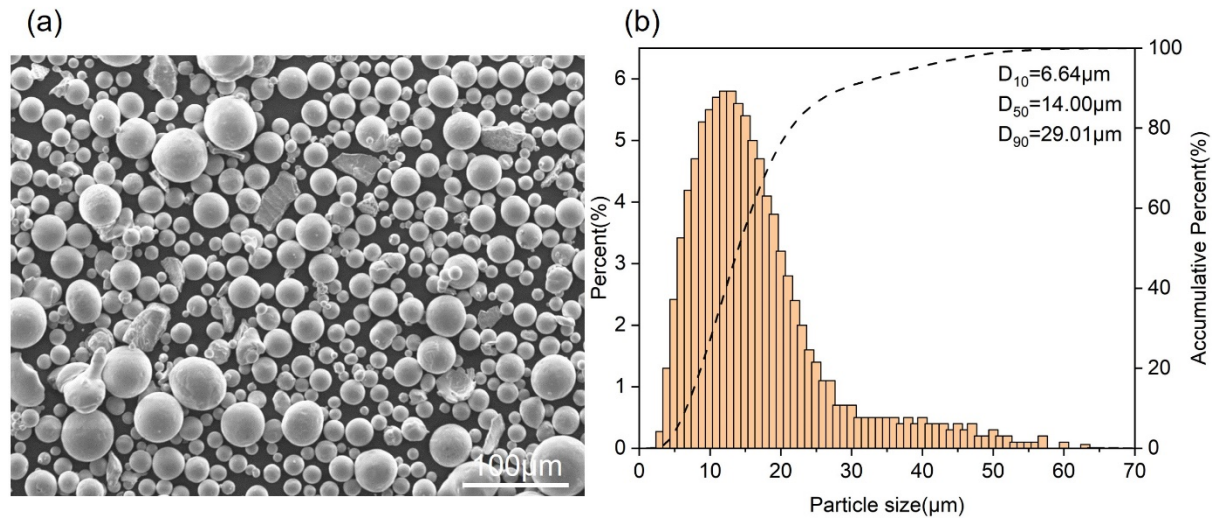


**Fig. 1** Characterization of pure copper powders. (a) SEM morphology of pure copper powders. (b) particle size distribution
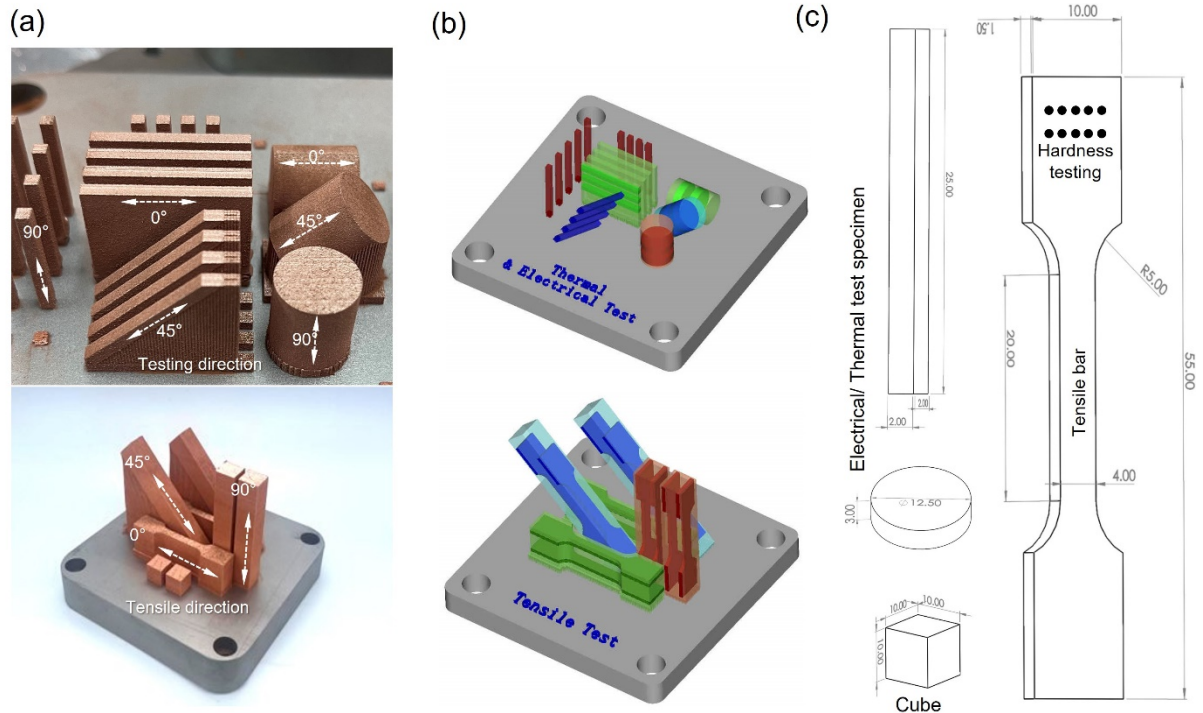
**Fig. 2** Definition in sample fabrication and measurement. (a) as-printed bulk samples with 0°/45°/90° orientation, (b) Testing samples layout on the building platform, (c) Dimension specification of samples for various tests.
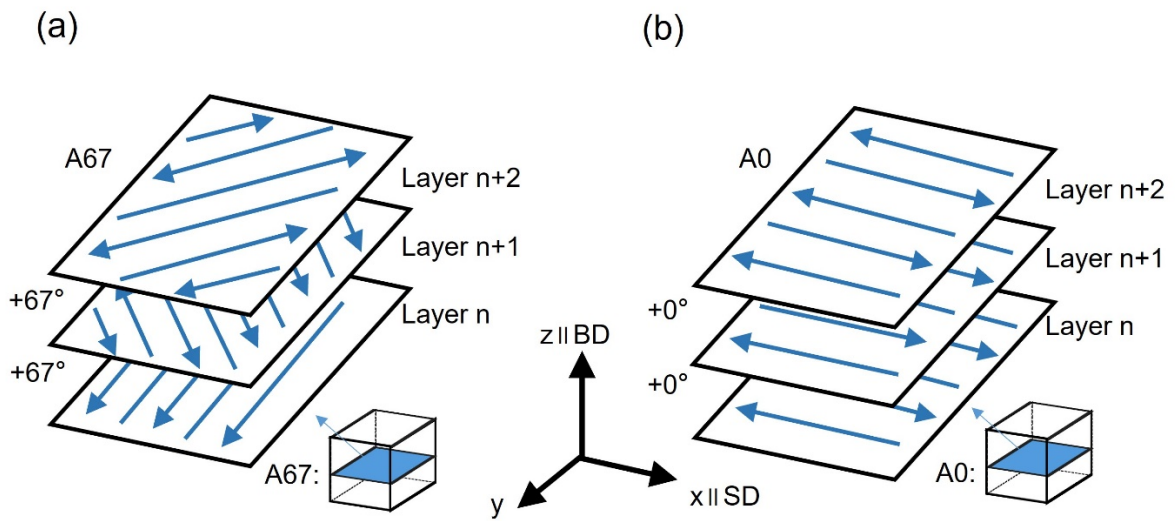


**Fig. 3** Two types of scan strategy. (a) 67° rotation angle - A67, (b) 0° rotation angle - A0

**Table. 1** Chemical composition of as-received Pure Cu powder

| Element | Cu | Fe | Zn | Pb | Al | P | Sn | Cd | O |
|---|---|---|---|---|---|---|---|---|---|
| wt. % | Bal. | 0.0125 | 0.015 | 0.0048 | 0.015 | 0.021 | 0.030 | 0.016 | 0.09 |

**Table. 2** The sample fabrication remarks

| Sample remarks | Power(W) | Scan speed (mm/s) | $E_l$ (J/m) | Scan rotation angle | Testing/tensile direction |
|---|---|---|---|---|---|
| A0-0° | 220 | 600 | 367 | 0° | 0° |
| A0-45° | 220 | 600 | 367 | 0° | 45° |
| A0-90° | 220 | 600 | 367 | 0° | 90° |
| A67-0° | 220 | 600 | 367 | 67° | 0° |
| A67-45° | 220 | 600 | 367 | 67° | 45° |
| A67-90° | 220 | 600 | 367 | 67° | 90° |
| AP-A67 (as-printed) | 220 | 600 | 367 | 67° | 0° |
| HP-A67 (high-power) | 260 | 600 | 433 | 67° | 0° |
| HS-A67 (high-speed) | 220 | 800 | 275 | 67° | 0° |

## 2.2 Characterisation

The morphologies of the original powders and the fracture surface of the tensile bars were studied by SEM (JCM-6000Plus). The OM morphology study was conducted on an RH-2000 high-resolution 3D microscope (Hirox). Before observation, the samples were ground, polished, and etched with an etching solution (5 g FeCl$_3$, 85 mL ethanol, and 15 mL HCl). The grain structure and texture studies were conducted on an EBSD system (EDAX Velocity Plus), using a step size of 0.5 μm and a scan area of 200 × 200 μm$^2$. MTEX 5.7.0, an open-source Matlab toolbox, was used to analyse the EBSD data [34]. Grain boundaries (GB) are defined according to their misorientation angle. The low-angle GBs (LAGBs) are with misorientation angles of 2°–15° and the

high-angle GBs (HAGBs) are with misorientation angles exceeding 15°. The grain size is determined by the HAGBs. The dislocation density was measured by using Williamson-Hall method [35]. X-ray diffraction (XRD) patterns were used to calculate the internal strain of samples. XRD measurements were conducted by a high resolution Rigaku SmartLab X-ray diffractometer with the 2θ angle range from 20 ° to 100 °. The step size was 0.02° and scan speed is 0.1°/min. The instrumental broadening was corrected using a strain-free Si powder as the reference. The microhardness of the samples was tested using a hardness tester (Decca HV-1000) at a load of 200 g for 10 s. The tensile bars (before being subjected to the tensile tests at a constant speed of 0.9 mm/min) were used to obtain the hardness at 0°, 45°, and 90° orientations. The test surfaces are shown in Fig. 2c; for example, the microhardness of the 90° samples was defined as the hardness at the side surface of the tensile bars oriented at 90°. Testing was conducted at ten testing points on each surface, and the average hardness was recorded. The tests under each condition were repeated on three tensile bars. The EC was measured using a micro-ohmmeter that had an accuracy of 0.05% and a sensitivity of 1 μΩ. The TC was measured using a light flash apparatus (LFA467, NETZSCH) at 25°C. These electrical and thermal tests conformed to their respective standards. For testing details, please refer to the previous work [26]. The EC and TC tests were conducted on three samples to ensure repeatability. Before the mechanical and EC and TC tests, the samples were ground and polished to eliminate errors caused by rough surfaces.

## 3. Results

### 3.1 Microstructure of HP-LPBFed pure Cu samples

Pure Cu samples were fabricated using the process window optimised in the previous work [26]. These samples (tensile bars, EC testing bars, and TC testing samples of various grain orientations) which were also used for evaluating anisotropy are defined in Fig. 2a. All of the samples had an RD higher than 99.5%. To reveal the influence of grain morphology on samples' EC, TC, mechanical properties, and anisotropy, two scan rotating angles (0° and 67°) were applied to print samples with different microstructures; these samples are hereinafter referred to as samples A0 and A67 (Table. 2).

Fig. 4 characterises the microstructure of the samples..The side cross-section of the A67 sample, characterised by OM, is presented in Fig. 4d, which contains grains with various orientations (arrows). Furthermore, it could be seen that numerous long fine grains had grown from the bottom of the molten pool and penetrated several upper layers (dashed lines). In the grain orientation map (Fig. 4e), some of the irregular grains were arranged in a chevron pattern (the red lines in Fig. 4f), whose asymmetry was due to the laser scan sequence [36] whereas the other grains were a mixture of fine-equiaxed and elongated grains. Chevron pattern in the overlapping zones between the melt pools has been reported in LPBFed components including stainless steel 316L, AlSi10Mg [27, 36, 37]. It is attributed to the continuous competition between epitaxial growth and thermal gradient.

Fig. 4g presents the horizontal-section morphology of the as-printed samples,

wherein mirrored 'S'-shaped grains were seen in neighbouring laser tracks. The dashed curves in Fig. 4h illustrate the obvious grain orientation arrangement on the top surface. Most of the grains were restricted to within the scan tracks. The formation of S-shaped grains has been reported by many other studies [38], and occurs via the remelting of neighbouring laser tracks with various scan orientations. This type of remelting was also responsible for the formation of the chevron-patterned grains on the side surface [36]. Therefore, the S-shaped grains on the top surface and the chevron-patterned grains on the side surface represented different cross-sections of the same grains, as indicated by the shaded patterns in Fig. 4f and i.

When the scan rotation angle was 0°, symmetrical columnar grains were more frequently generated from the bottom of the molten pool than at 67° scan rotation angles (Fig. 4j). The grains were arranged along the BD as the thermal gradient was equal across different layers. Fig. 4k shows that the grains grew continuously across the layers, whereas clear boundaries were evident along the BD. The shaded area in Fig. 4l indicates the A0 sample and its typical grains: columnar grains with a high aspect ratio.

Fig. 4m shows the representative inverse pole figure (IPF) of the side surface of the A0 sample, which suggests that it had a texture of <110>//BD with an intensity of 4.5. The side surface of the A67 sample also has the same texture in the BD, with a minimum intensity of 2 (Table. 3). Fig. 4n shows the distribution of large grains extracted from raw EBSD data. The average grain sizes in the side cross-sections of the A67 and A0 samples were 7.52 and 7.42 μm, respectively, which were larger than

those in the top cross-sections of A67 samples (5.40 μm). The A67 samples had finer

grains on their top cross-sections than on their side cross-sections, indicating that the

general grain morphology of A67 was quasi-columnar.

Fig. 4f, i, l illustrates the distribution of the LAGBs and the HAGBs; these data

were obtained from the raw EBSD data of the scan area. Fig. 4o shows that the A67

and A0 samples exhibited a similar length density and LAGB/HAGB fraction,

indicating that these two types of samples primarily differ in their grain shape.

**Table. 3** The statistical EBSD results of pure copper samples

| Items | A67-side | A67-top | A0-side |
| --- | --- | --- | --- |
| Intensity//BD | 2 | 2.4 | 4.5 |
| Length density (LAGB/HAGB, μm-1) | 1.57/0.58 | 1.69/0.99 | 1.55/0.43 |
| Fraction (LAGB/HAGB, %) | 73.0/27.0 | 63.1/36.9 | 78.3/21.7 |
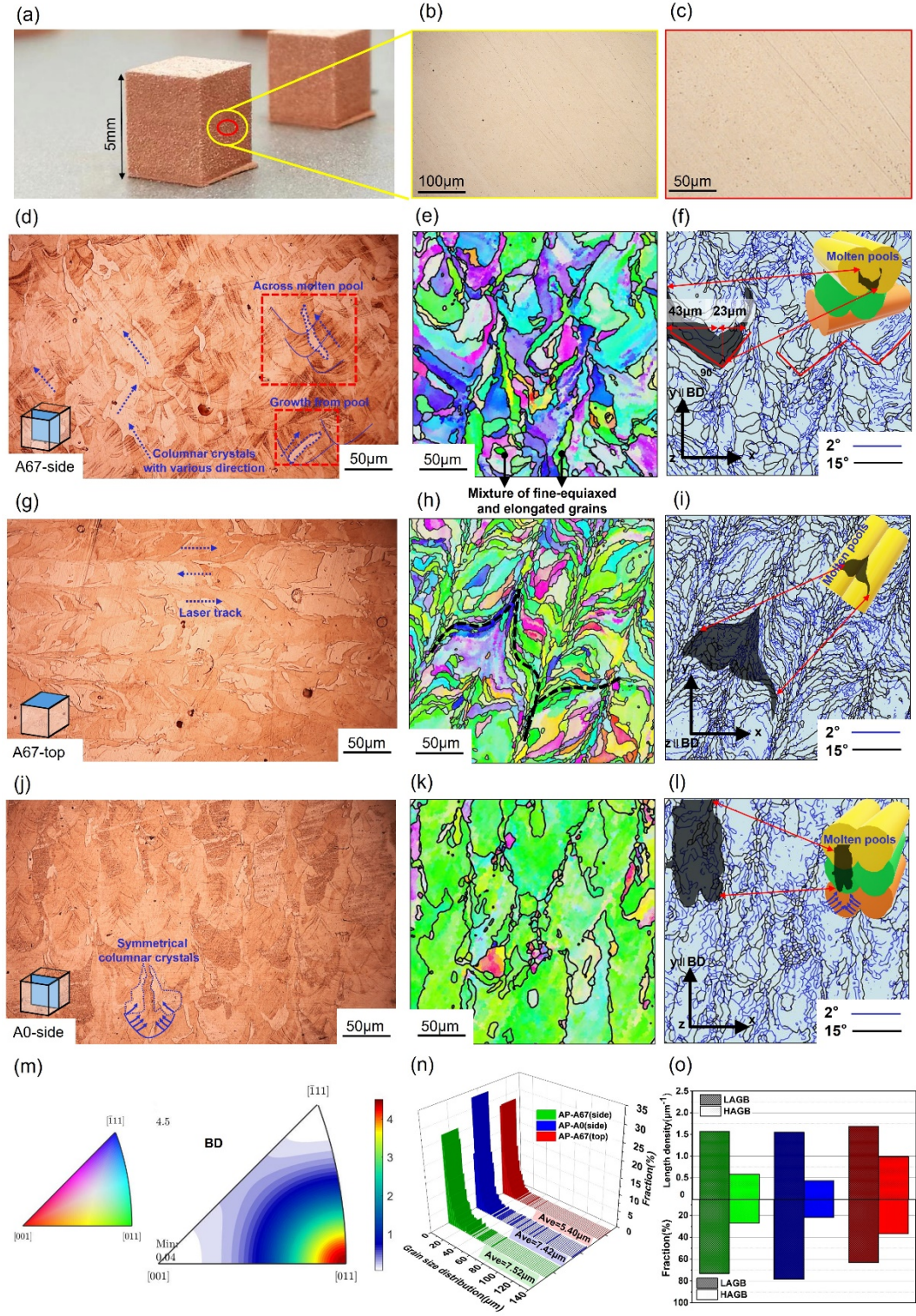
**Fig. 4** Microstructure characterisation of HP-LPBFed pure Cu samples. (a–c) morphologies of as-printed samples at different magnifications, (d–f) side surface of the A67 sample, (g–i) top surface of the A67 sample, (j–l) side surface of the A0 sample. (d, g, j) OM images, (e, h, k) EBSD grain orientation maps and (f, i, l) GB distribution maps. (m) representative IPF map, (n) grain size distribution of as-printed pure Cu samples, (o) GB length density and HAGB/LAGB fraction of as-printed pure Cu samples.

To comprehensively characterise the microstructure of the A0 and A67 samples, we extracted grain morphology data from these samples' three crystal structure maps (Fig. 5). The linear density of GBs was determined by the line intercept method [39], which identifies the difference in the GB distribution in the 0°, 45° and 90° grain orientations. The grain-size aspect ratios are summarised in Fig. 5b. The grain-size aspect ratio of the A0 sample was greater than 2.0, while that of the A67 sample was 1.2. Figs. 5c and d indicate that the A67 and A0 samples had 'chevron' and 'cylinder' grain morphologies, respectively.

In the A67 sample, there are more inclined GBs in the 45° orientation than in other orientations. In addition, the main thermal gradient in the BD induced the formation of quasi-columnar grains (aspect ratio ~1.2), and thus a higher GB density in the 0° grain orientation than in the 90° grain orientation (Fig. 5a). However, in the A0 sample, the scan tracks of adjacent layers overlapped, and thus there was a stable thermal gradient in the BD. Thus, the grains in the newest layer were able to easily nucleate on grains in the preceding layer, and these new grains inherited the orientation of those in the preceding layer; this resulted in the epitaxial growth of long columnar grains (Fig. 4k). Consequently, the GB density of grains in the A0 sample decreased from the 0° to the 90° orientation (Fig. 5a).
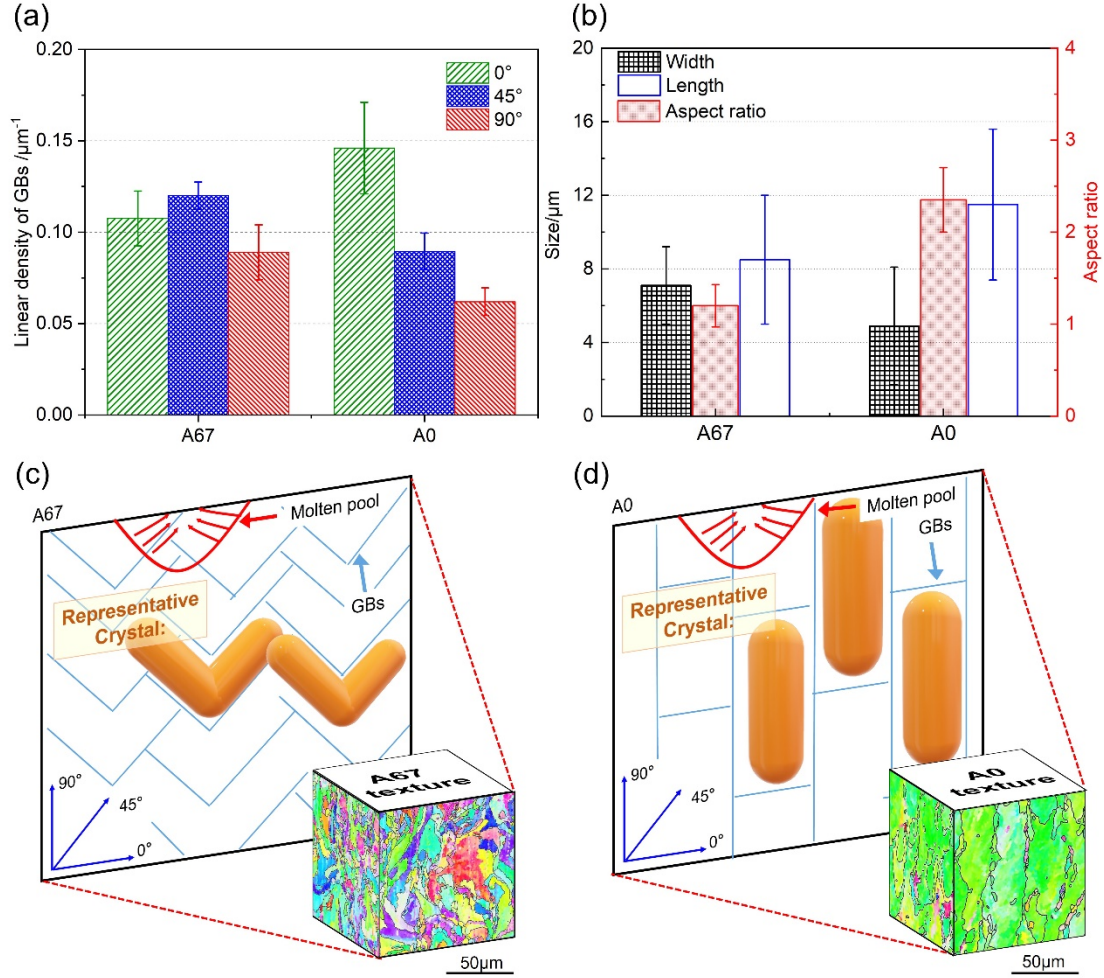
Fig. 5 Grain morphology characterisation of the A67 and A0. (a) Linear GB density; (b) grain size and aspect ratio; (c- d) representative grain morphology of (c) A67 and (d) A0 samples.

## 3.2 Properties of HP-LPBFed pure Cu samples

As shown in Fig. 6, HP-LPBFed pure Cu samples exhibited anisotropy in their mechanical properties, as evident in the stress–strain curves of as-printed pure Cu tensile bars A0 and A67 (Table. 4). The YS of all tested samples was over three times higher than that of annealed pure Cu samples (67 MPa) [14]. The A67-90° sample had an elongation at failure of 33.5%, which was higher than those of the A67-0° and A67-45° samples. In contrast, the A67-0° and A67-45° samples had a higher true YS (~229 MPa) and ultimate tensile strength (UTS, ~378 MPa) than those of the A67-90°

sample. The strength and ductility of the A0 samples were both lower than those of A67 samples.

To clarify the deformation behaviour, Fig. 6d plots the evolution of normalised strain hardening rate ($\theta$) [40] , which was calculated using as follows (Eq. (1)):

$$\theta = \frac{1}{\sigma}\left(\frac{d\sigma}{d\varepsilon}\right)(1)$$

where $\sigma$ and $\varepsilon$ are the true stress and true strain, respectively. All samples showed a rapid decrease in $\theta$ in the first stage after yielding. Thereafter, their $\theta$ decreased slowly before post-necking in the second stage. Post-necking occurs when $\theta < 1$ [41]. The grain orientation (0°, 45°, or 90°) affected the BD and thus the tensile test results, as a grain orientation of 0° resulted in the highest hardening rate in the second stage, whereas a grain orientation of 90° resulted in the lowest hardening rate in the second stage. The dashed lines represent the A0 samples, which showed a lower hardening rate in the first stage (see arrows) at grain orientations of 45° and 90° but not at a grain orientation of 0°.

To further understand the deformation behaviours, the instant work-hardening exponent $n$ was calculated based on the Hollomon equation, as follows [42]:

$$n = \frac{d(ln\sigma)}{d(ln\varepsilon)}(2)$$

All samples had a similar trend for $n$ (Fig. 6e): a steady increase with stress after yielding. At post-necking, $n$ reached a maximum and decreased rapidly thereafter. In the starting stage, the tensile bars with a grain orientation of 0° and 90° exhibited a similar $n$, whereas those with a grain orientation of 45° exhibited a lower $n$. In the final stage (i.e., before reaching the maximum $n$), the growth rate of $n$ for the tensile

bars with a grain orientation of 0° was lower than that for those with a grain orientation of 45°, because of which the latter were ultimately larger than the former. The A0 samples had an $n$ (dashed lines) that was generally less than that of the A67 samples, but with a similar trend at each grain orientation (0°, 45°, and 90°). Fig. 6c–f plots the anisotropy ratio of the tensile properties of the A0 and A67 samples, benchmarked against the grain orientation of 0°, for which the anisotropy ratio is 1. The ductility of the A67 sample was weakly anisotropic comparing to that of the A0 sample, and the YS and UTS had different anisotropic ratios in each of the three grain orientations. The anisotropy ratios for ductility varied by as much as ~60% and ~35% in the A67 and A0 samples, respectively.

Fig. 6g presents the microhardness of the samples at different orientations. In the A67 samples, the average microhardness decreased from 98 to 95.7 HV as their grain orientation varied from 0° to 90°. Fig. 6h shows that the anisotropy ratio of microhardness for the A67 sample (1.000:0.986:0.976) was less than that of the A0 sample (1.000:0.981:0.959). Although the average has the different value of samples at different orientations, the error bar makes the results insufficient to show that the microhardness of Cu is anisotropic. The variation of samples on the hardness is negligible. Furthermore, The microhardness values of pure Cu components fabricated via EB-PBF [14], cLPBF [19] and annealing [14] were reported to be 50, 66, and 46 HV, indicating that HP-LPBF produces pure Cu with the highest as-printed hardness yet reported for all the PBF processes.

Fig. 6i clarifies that the TC and EC of all samples were near-isotropic and that

they were not significantly influenced by the rotating angle or the BD. In the as-printed condition, the TC reached a maximum of ~383 W/m·K and the EC was approximately 96% of the IACS, which was 15% greater than IACS of samples reported in a previous study [26]. This increase was due to preheating the substrate to 100°C, as was suggested by others [43]. The EC and TC of HP-LPBFed pure Cu samples were close to the theoretical maxima for these values exhibited by C10100 oxygen-free electronic (OFE) Cu [1]. This shows that the columnar and twisty grains of the HP-LPBFed pure Cu samples did not lead to significantly anisotropic electrical and thermal properties. This is similar to the isotropic thermal and electrical properties of EB-PBFed pure Cu samples [14].
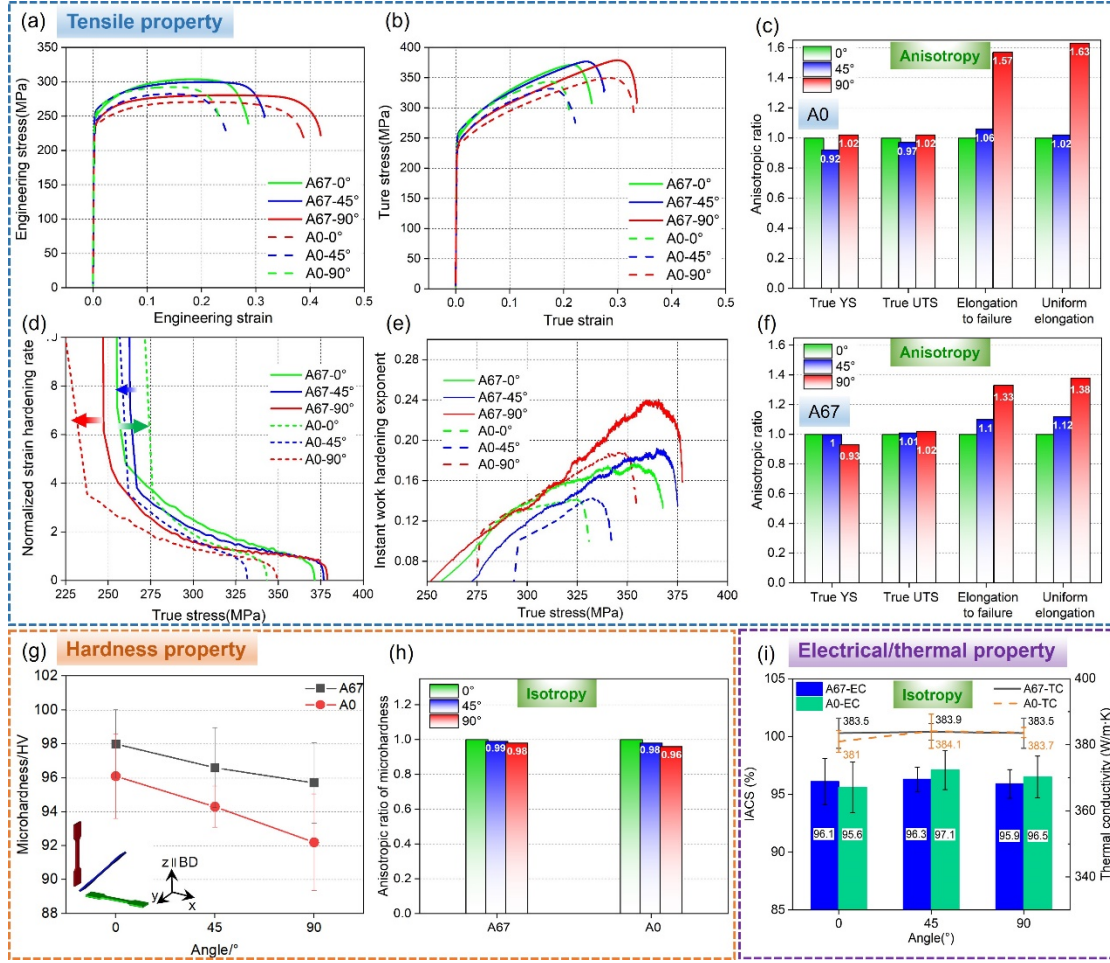
**Fig. 6** Properties of HP-LPBFed as-printed pure Cu A0 and A67 samples. (a) Engineering stress–strain curves; (b) true stress–strain curves; (d) normalised work-hardening rates; (e) instantaneous work-hardening exponents; (c- f) anisotropy ratios of with sample orientations of 0°, 45°, and 90° (anisotropy ratio at 0° = 1); (g) micro-hardness at sample orientations of 0°, 45°, and 90°; (h) anisotropy ratios at sample orientations of 0°, 45°, and 90° (the anisotropy ratio at orientation 0° = 1); and (i) thermal and electrical properties at different orientations.

**Table. 4** Mechanical properties of HP-LPBFed pure Cu samples

| Sample | True YS (MPa) | True UTS (MPa) | Elongation to failure (%) | Uniform elongation (%) |
|--------|---------------|----------------|---------------------------|------------------------|
| A0-0° | 213 ± 9 | 343 ± 13 | 20.9 ± 0.9 | 17.2 ± 1.1 |
| A0-45° | 195 ± 3 | 332 ± 18 | 22.1 ± 1.3 | 17.5 ± 1.4 |
| A0-90° | 217 ± 5 | 350 ± 16 | 32.9 ± 2.3 | 28.1 ± 2.5 |

| | | | | |
|---|---|---|---|---|
| A67-0° | 217 ± 11 | 371 ± 6 | 25.2 ± 2.1 | 21.6 ± 1.5 |
| A67-45° | 218 ± 6 | 376 ± 11 | 27.6 ± 1.6 | 24.2 ± 2 |
| A67-90° | 201 ± 8 | 378 ± 7 | 33.5 ± 1.5 | 29.9± 1.3 |

### 3.3 Fine grain strengthening in HP-LPBFed samples

Fig. 7a, b illustrates the tensile curves of groups of HP-LPBFed pure Cu samples generated using different process parameters (Table. 2). $E_l$ is often used to determine the optimal window for processing parameters, [44] as the higher the $E_l$, the higher the temperature of the molten pool and the slower the cooling rate during solidification, all of which lead to a larger grain size. In crystal structure maps, the average grain size of sample HP-A67, which was generated at a higher-than-normal power and speed (260 W and 600 mm/s, respectively) was 8.43 μm, whereas that of sample AP-A67, which was generated at a normal power/speed (220 W and 600 mm/s, respectively) was 7.52 μm. The average grain size of sample HS-A67 (220 W and 800 mm/s) was 5.46 μm, and these fine grains gave it higher strength and thus better work-hardening behaviour than other samples, and relatively high strength and elongation. Although the RD of sample HS-A67 is ~99.5%, it was also susceptible to lack-of-fusion defects which is hard to be revealed by RD [26].

Fig. 7c–f shows the fracture morphology of the HP-LPBFed as-printed pure Cu samples. The necking phenomenon was seen in all of the samples regardless of the scanning rotating angle (Fig. 7c). The typical fracture morphology, captured through SEM, is shown in Fig. 7d, wherein the dimples and river pattern can be seen on the

fracture surface. The as-printed samples were classified as exhibiting a mixed ductile–brittle fracture mode [45]. At higher magnification (Fig. 7e), pores of size ~1 μm were visible among the dimples. The dimples (100–400 nm) in the samples were smaller than those in cLPBFed Cu samples [45, 46].
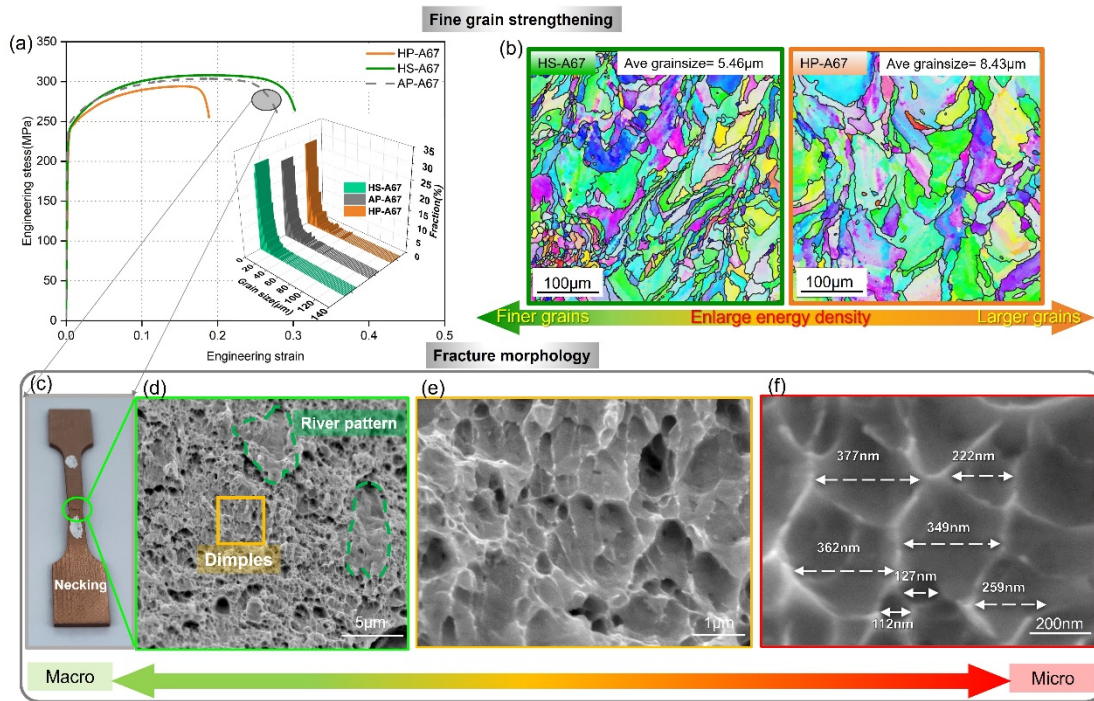


**Fig. 7** Influence of grain size on the tensile property of HP-LPBF as-printed pure Cu samples. (a) Typical tensile stress–strain curves of samples fabricated using various values of processing parameters and exhibiting various grain sizes; (b) IPF maps of HP- and HS-A67 samples. (c- f) Fracture morphology of the samples observed via SEM at different magnification.

## 4. Discussion

### 4.1 Yield strength

The YS of polycrystalline materials is related to their available slip systems, the geometrical constraints on their GBs, [47] and the dislocation density [44]. The Schmid factor is often used to describe the activation of slip systems of grains with

22

different orientations and the anisotropy of polycrystals. The Schmid factors of the A67 and A0 samples with grain orientations of 0°, 45°, and 90°, which were extracted from EBSD data are shown in Fig. 8. On average, the Schmid factor in the A0 sample with a grain orientation of 45° was the largest (0.4608), which was consistent with its lowest YS of 195 MPa (Table. 4). However, the YS (~217 MPa) in the A0 sample with a grain orientation of 90° was nearly the same (~213MPa) in the 0° direction, while the Schmid factor at these two orientations has a 5% difference. Besides, the A67 sample with a grain orientation of 45° sample exhibited the largest Schmid factor of 0.4545, but its corresponding YS was greater than those of the samples with a grain orientation of 0° or 90°. These two exceptions suggest that the Schmid factor alone may not be sufficient to account for the anisotropy of YS. The anisotropy of GB morphology must also be considered.
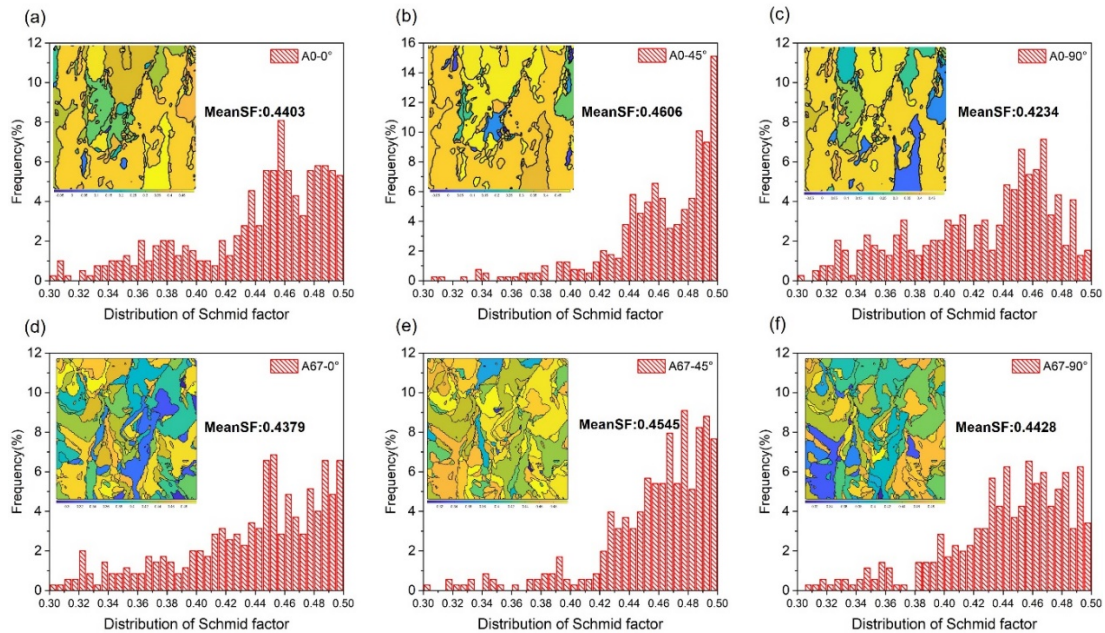


**Fig. 8** Schmid factor distribution and mean Schmid factor of samples. (a) A67-0°, (b) A67-45°, (c) A67-90°, (d) A0-0°, (e) A0-45°, (f) A0-90°.

The GB strengthening phenomenon is largely explained by the Hall–Petch relationship [48]. That is, the more GBs that need to be overcome in the loading direction, the larger the force that is needed to cause the material to yield during deformation [49]. Because GBs typically act as obstacles to dislocation movement, dislocations build up at GBs in material, which ultimately enhances its strength. The GB linear density distribution in the 0°, 45°, and 90° orientations in the A0 and A67 samples was obtained from Fig. 5, and explains why the A67-45° sample had the highest YS: it had the highest GB density.

The strengthening of pure Cu could be attributed to the GB strengthening ($\Delta\sigma_{GB}$), dislocation strengthening ($\Delta\sigma_{dis}$). Therefore, the YS ($\Delta\sigma_{YS}$) can be expressed as[50]:

$$\sigma_{YS} = \sigma_0 + \Delta\sigma_{GB} + \Delta\sigma_{dis} \quad (3)$$

where $\sigma_0$ is the intrinsic YS of Cu which is related to the friction of lattice. This strength was estimated to be 61.8MPa[50]. Moreover, GB strengthening ($\Delta\sigma_{GB}$) can be estimated using Hall-Petch relationship:

$$\Delta\sigma_{GB} = \frac{k_{HP}}{\sqrt{d}} \quad (4)$$

where $k_{HP}$ is the materials specific Hall-Petch coefficient (0.11MPa·$\sqrt{m}$), $d$ is the grain size (~7μm). Hence, the contribution of GB strengthening on the YS could be calculated to be 41.5MPa. In addition to GB strengthening, the dislocation strengthening is also a dominant factor of increasing YS. $\Delta\sigma_{dis}$ can be estimated by the Bailey-Hirsch relationship:

$$\Delta\sigma_{dis} = M\alpha Gb\sqrt{\rho} \quad (5)$$

where $M$ is the Taylor factor ~3.06 for face-centred cubic (FCC) Cu, $\alpha$ is the

geometrical factor for FCC metals (0.2), $G$ is the shear modulus of Cu (48.3GPa), $b$ is the burgers vectors of Cu (0.256nm), and $\rho$ is the dislocation density. Dislocation density was measured using Williamson and Hall method[51]:

$$\delta \cos\theta = \frac{\lambda}{D} + 2\varepsilon \sin\theta \quad (6)$$

Where $\delta$ is the physical broadening of full width at half maximum (FWHM) of the diffraction peak, $\theta$ is the diffraction angle, $\lambda$ is the wavelength of radiation, $D$ is the grain size, and $\varepsilon$ is the internal strain. The $\varepsilon$ and $D$ can be acquired by using linear fit. The contribution of grain size on the peak broadening is negligible due to the wavelength $\lambda_{K\alpha1}$=0.154nm and $D$= ~7μm. Hence, the term of $\frac{\lambda}{D}$ can be set to be zero[35]. Four planes of (111), (200), (220) and (311) were used for linear fitting [44]. The strain $\varepsilon$ can be estimated to be 0.099% shown in Fig. 9. The dislocation density $\rho$ could be calculated:

$$\rho = k \frac{\varepsilon^2}{b^2} \quad (7)$$

Where $k$=16.1 for FCC Cu, and $b$ is the Burgers vector. Dislocation density was estimated to be $1.99 \times 10^{14}$ m$^{-2}$. Furthermore, Fig.10(a)-(c) show the geometrically necessary dislocation (GND) maps computed from the raw EBSD data on corresponding samples. GND density of cross-section of A67/A0 samples is in the order of ~$1 \times 10^{14}$ m$^{-2}$, which demonstrates that the measurements by XRD are reasonable. Therefore, according to Eq(5), the strengthening increase by dislocation $\Delta\sigma_{dis}$ was estimated to be 106.7MPa. Overall, we estimate $\sigma_{YS}$ of 210MPa in accord with the experimental measurements (200~220MPa).
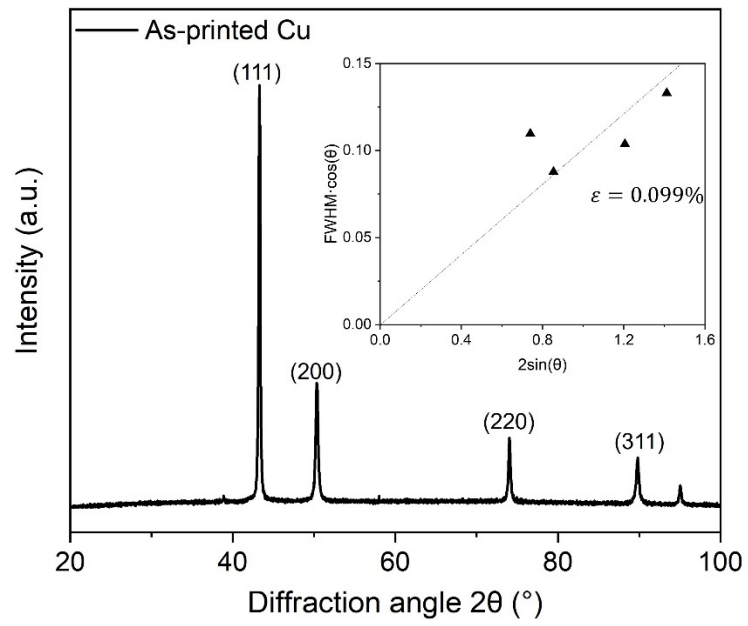
Fig. 9 The XRD profiles of as-printed Cu and Williamson-Hall plot for the diffraction
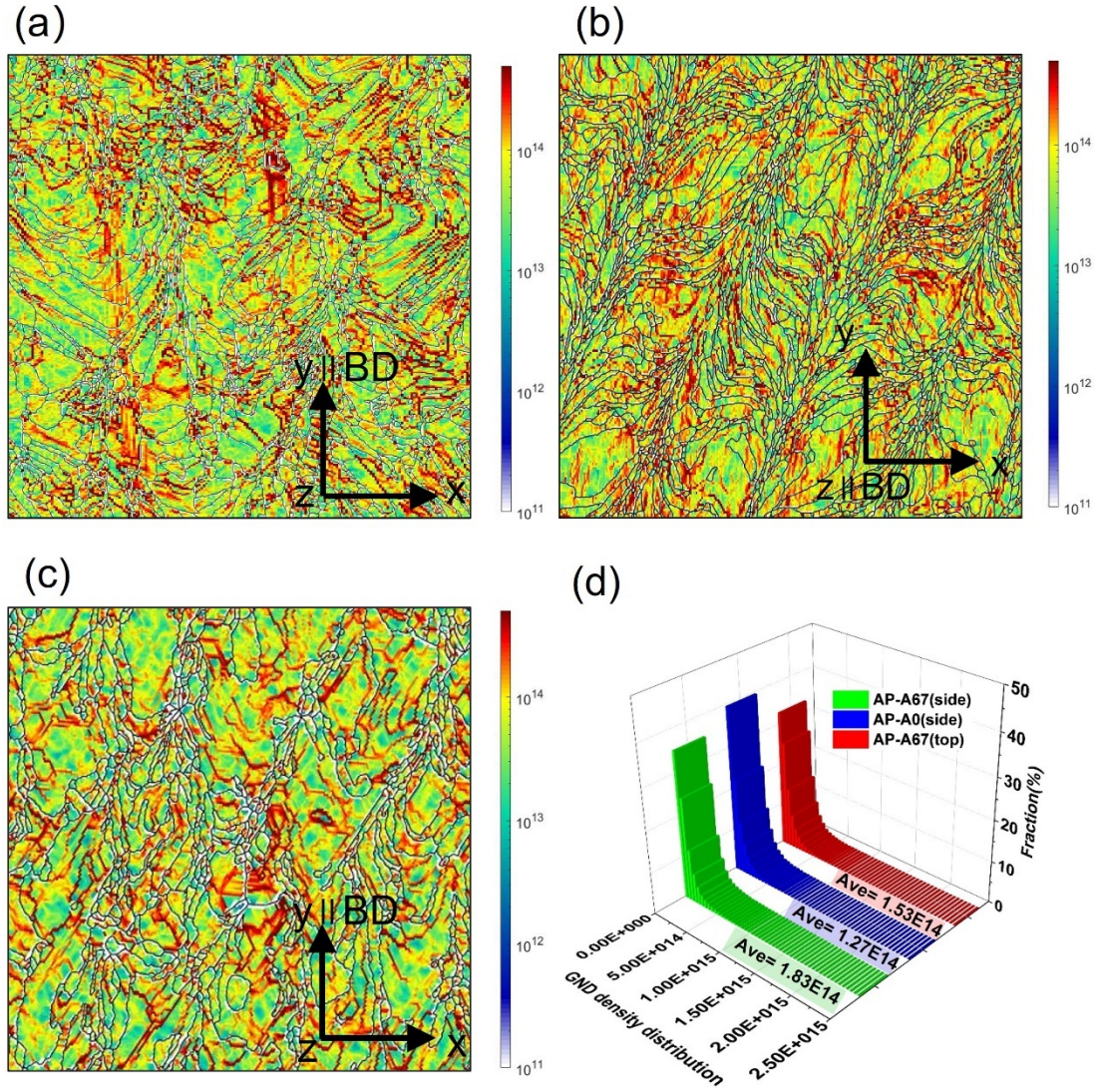
pattern

Fig. 10 (a)-(c) GND maps of side surface of the A67sample, top surface of the A67 sample, side surface of the A0 sample, (d) GND density distribution on corresponding samples

## 4.2 Ductility and work hardening behavior

The A67 samples generally has higher ductility (25.2%–33.5%) than the A0 samples (20.9%–32.9%), which is attributable to grain refinement [52]. Fine grains can easily accommodate deformation and inhibit microcrack generation. In addition, molten pool boundaries were reported to have weak binding forces [53], and thus a

coarse grain zone, leading to these boundaries failing rather than GBs. The twisty molten pool of the A67 samples introduced multi-angle boundaries, which prevented the formation of cracks and thus enhanced these samples' ductility [54], whereas the unidirectional distribution of grains in the A0 samples resulted in uneven deformation and crack initiation.

Regarding the anisotropic tensile behaviour of the LPBF samples, a 90° grain orientation has been reported to have a higher elongation than a 0° grain orientation [27, 53, 55]. The anisotropic ductility of LPBFed 316L stainless steel is often due to twinning deformation [47, 55]. However, many reports [56-58] have demonstrated that due to high stacking-fault energy, deformation twinning of Cu rarely occurs at room temperature and at low strain rates, unless prior severe plastic deformation has occurred [56]. Therefore, in the as-printed Cu, dislocation slipping, not twinning, was the dominant deformation mechanism; that is, the columnar grains were responsible for the anisotropic deformation behaviour. The higher GB density at grain orientations of 0° than at grain orientations of 90° is because the former generates more barriers that the dislocations needed to overcome. As discussed in the previous section, dislocation density is the dominant strengthening mechanism in pure Cu, and the initial dislocation densities of all HP-LPBFed samples in this work were almost the same. However, the hardening stage differed for the A0 and A67 samples and the HP and HS samples, which was due to the key roles played by the accumulation, storage, and nucleation of dislocation. A higher GB density generated more dislocations in the plastic deformation stage and enhanced the work-hardening rate. Therefore, the

anisotropic ductility can be attributed to the different GB density in different grain orientations leading to various mean free paths for the dislocations.

### 4.3 Microhardness

The Hall–Petch relationship is usually applied to explain the relationship between grain size and hardness, as follows (Eq. (4)) [59]:

$$H = H_0 + kd^{-\frac{1}{2}} \quad (4)$$

where $H$ is microhardness, $H_0$ and $k$ are material constants, and $d$ is the grain size of the material. Although the EBSD results in Fig. 4 show that the top surface (~5μm) had finer grains than the side surface (~7μm), the highly nonuniformity of grain size in a local area makes the microhardness variation induced by different surface is negligible shown in Fig. 6(g). The microhardness mostly ranges from 90~98HV and the variation in the same surface of samples is about ~6HV. Therefore, we conclude the Cu components are isotropic in microharness.

### 4.4 Electrical and thermal conductivity

The EC and TC of pure Cu is related to its defects, namely GBs, dislocations, and other electron scattering-induced defects [29]. If we ignore the vacancies and impurity elements (which are minor and not applicable to this case), the anisotropy of EC and TC in LPBFed Cu can be derived from the non-uniformity of GBs and dislocations. According to the Matthiessen rule [60], the resistivity of pure Cu, $\rho_0$, can be expressed as

$$\rho_0 = \rho_t + \rho_{GBs} + \rho_{dislocations} + \rho_{others} \quad (5)$$

where $\rho_t$ is the resistivity corresponding to the temperature, $\rho_{GBs}$ represents the resistivity induced by the GBs, $\rho_{dislocations}$ is the resistivity related to dislocations and $\rho_{others}$ is the resistivity related to impurities and voids. $\rho_{dislocations}$ is influenced by the dislocation density, which is $1 \times 10^{14}$–$1 \times 10^{15}$ m$^{-2}$ in as-printed pure Cu [44]. However, a dislocation density of 1 cm$^{-2}$ leads to a resistivity of only approximately $1.5 \times 10^{-13}$ μΩ·cm [61], and the dislocations contribute less than 0.9% of the IACS. Similarly, $\rho_{GBs}$ can be written as [61]

$$\rho_{GBs} = \frac{3}{2} \cdot \frac{\lambda}{D} \cdot \frac{R}{1-R} \cdot \rho_0 \quad (6)$$

where $R$ is the reflection coefficient, which is related to the characteristics of the GB; $\lambda$ is the mean free path of the electrons (~40 nm); $D$ is the grain size; and $\rho_0$ is the bulk resistivity of pure Cu (1.7 μΩ·cm). $R$ is reported in the literature to be 0.56 [62]. Therefore, $\rho_{GBs}$ was about 1.03% of the IACS for a grain size of 7.52 μm (Fig. 6k). Thus, the anisotropic fine grains exerted little influence on the EC. In pure Cu, the TC and EC follow the Wiedemann–Franz relationship [19, 63] , because the carriers follow the same transition mechanism. Thus, both the TC and EC were excellent and near-isotropic in HP-LPBFed pure Cu samples.

### 4.5 Superior material properties of pure copper achieved by HP-LPBF

The first superiority of HP-LPBF is low requirement for the laser power. The fine beam enables the focus of energy and sufficient melting of solid Cu. Furthermore, each layer can be well fused by utilizing the thin layer of 10μm and more absorptivity

of laser energy can be achieved by fine powder ($D_{50}$~14µm). In the previous work, a fine laser beam size of 35 µm has been employed to fabricate pure Cu parts by Silbernagel et. al [3]. However, the 30-60 µm layer thickness and a large average particle size of 38 µm, which require a high energy input, result in an insufficient melting and lack-of-fusion microstructure with RD of 85.8%. Overall, the HP-LPBF properly combined the features (fine beam, thin layer thickness, and fine powders) to realize the defect-free LPBFed Cu in this work.

In terms of microstructure, the crystal structure in PBFed samples largely depends on epitaxial growth, which is controlled by the thermal gradient during processing, and the nucleation, which is influenced by the grains in the preceding solidified layers [36]. Because LPBF is a bottom-up and layer-by-layer process, thermal gradient in the BD is inevitable. Hence, columnar grains are common in PBF processes [13, 63, 64]. Furthermore, the different rotating angles in samples A67 and A0 led to differences in their nucleation characteristics, which ultimately affected their microstructure. Given the use of thin layers (10 µm) and a fine laser beam (25 µm), the molten pools in the HP-LPBF process were only ~100 µm deep [26]. In contrast, cLPBFed pure Cu samples obtained with thicker layers (30 µm) and a thicker laser beam (37.5 µm) had molten pools depth ~400 µm [19]. Thus, relatively fine grains in HP-LPBF are a result of its smaller molten pools and higher cooling rates [27].

Despite the fine grains, a comparison between the A67 and A0 samples reveals that grains with different aspect ratios influenced the anisotropy of the mechanical

properties of the samples, including their ductility and strength. During layer-by-layer processes, the vertical thermal gradient along BD is stable. In addition, as reported [17], the laser scan enables the horizontal thermal gradient along the moving direction of molten pools. Hence, the rotation angle makes scan direction different and thermal gradient complicated, which realizes the different direction of grain growth in the A67 samples. However, there was a more stable thermal gradient in A0 samples without 67 degrees rotation for each layer. As a result, the A0 samples have more long and straight grains with higher aspect ratios.

In summary, pure Cu samples fabricated by a HP-LPBF process have demonstrated better mechanical properties, TC and EC than those fabricated by other PBF processes (Fig. 11). Fig. 11a shows the trade-off between UTS and elongation of samples obtained by the HP-LPBF process and those obtained via other PBF techniques [10, 14, 19, 25, 44-46]. The yellow region indicates the properties of OFE Cu [1]; as can be seen most of as-printed PBFed samples had better mechanical properties than OFE Cu. Thus, with respect to the UTS–elongation trade-off, the HP-LPBFed samples had better mechanical properties than all previously reported PBFed samples. The EC and YS of the various samples are presented in Fig. 11b. Most studies have to make undesirable trade-off between these two properties, whereas the HP-LPBFed pure Cu presented in this work simultaneously achieved high EC and high YS, highlighting its great potential in fabricating complex pure Cu samples with high performance requirement.
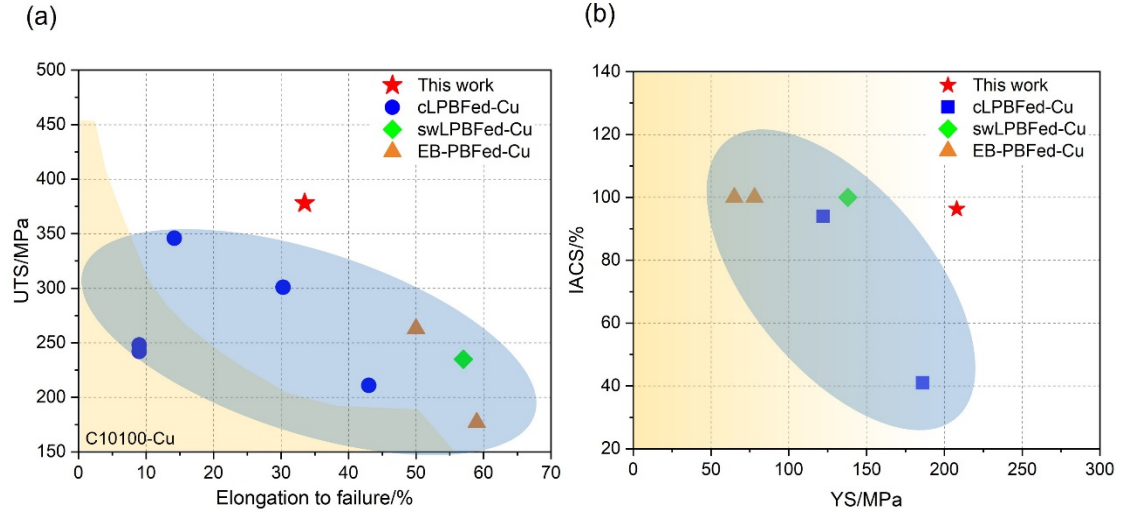
**Fig. 11** Comparison of pure Cu obtained by HP-LPBF and other PBF processes. (a) UTS vs. elongation-to-failure; (b) EC vs. YS.

## 5. Conclusion

By HP-LPBF with fine laser beam of 25μm and 10μm layer thickness, the high comprehensive performance of pure copper has been achieved with good thermal/electrical conductivity and mechanical property. Through rotating the scan directions between layers, the grain aspect ratio was reduced, and the mechanical properties were improved with weakened material anisotropy. The fine grain size of ~ 5μm are attributed to the smaller molten pool formed by HP-LPBF. The electrical and thermal performance of as-printed parts are close to the commercial pure copper in the annealed condition. Overall, the comprehensive performance of the pure copper fabricated by HP-LPBF outperforms those by other PBF techniques, which has great potentials in many exciting applications such as electromagnetics and thermal management. The main takeaways of this work are presented as follow:

1.  The high comprehensive properties of pure copper were realized by HP-LPBF with 25μm laser beam size, 10μm layer thickness, 5-30μm powder size: YS

~200MPa, UTS ~380MPa, total elongation ~40%, microhardness ~97 HV, thermal conductivity ~383W/m·K, and electrical conductivity ~96% IACS.

2. When rotation angle of 67° were applied, the grain morphology was twisty with higher GBs density along 45° direction. When the rotation angle was 0°, the grain morphology was straight. The GBs density ranking order is 0°>45°>90°. The variation of GBs density was responsible for the anisotropy of mechanical properties.

3. Strength has a similar anisotropic ratio in A67/A0 samples, which is related to the GBs density distribution. Ductility has anisotropy value of ~60% and ~35% in A67 and A0 respectively. The microhardness, thermal and electrical conductivity of HP-LPBFed pure copper is almost isotropic.

4. When parameters with different energy density were used, the grain size of as-printed pure copper vary. The finer the grain, the higher the strength and ductility.

**Acknowledgements**

**References**

[1] J.R. Davis, Copper and copper alloys, ASM international, 2001, 10.1361/caca2001p003

[2] C. Silbernagel, I. Ashcroft, P. Dickens, Electrical resistivity of additively manufactured AlSi10Mg for use in electric motors, Addit. Manuf. 21 (2018) 395-403, https://doi.org/10.1016/j.addma.2018.03.027

[3] C. Silbernagel, L. Gargalis, I. Ashcroft, Electrical resistivity of pure copper

processed by medium-powered laser powder bed fusion additive manufacturing for use in electromagnetic applications, Addit. Manuf. 29 (2019) 100831, 10.1016/j.addma.2019.100831

[4] T. Femmer, A.J. Kuehne, M.J.C.E.J. Wessling, Estimation of the structure dependent performance of 3-D rapid prototyped membranes, Chem. Eng. J. (Amsterdam, Neth.) 273 (2015) 438-445

[5] Z. Cheng, R. Xu, P.-X.J.I.J.o.H. Jiang, Morphology, flow and heat transfer in triply periodic minimal surface based porous structures, Int. J. Heat Mass Transfer 170 (2021) 120902

[6] L. Constantin, N. Kraiem, Z.P. Wu, Manufacturing of complex diamond-based composite structures via laser powder-bed fusion, Addit. Manuf. 40 (2021) 101927, 10.1016/j.addma.2021.101927

[7] S. Qu, J. Ding, X. Song, Achieving Triply Periodic Minimal Surface Thin-Walled Structures by Micro Laser Powder Bed Fusion Process, Micromachines 12(6) (2021) 705, 10.3390/mi12060705

[8] M. Zhang, Q. Yu, Z. Liu, 3D printed Mg-NiTi interpenetrating-phase composites with high strength, damping capacity, and energy absorption efficiency, Science Advances 6(19)    eaba5581, 10.1126/sciadv.aba5581

[9] X. Zheng, W. Smith, J. Jackson, Multiscale metallic metamaterials, Nature Materials 15(10) (2016) 1100-1106, 10.1038/nmat4694

[10] R. Guschlbauer, S. Momeni, F. Osmanlic, Process development of 99.95% pure copper processed via selective electron beam melting and its mechanical and physical properties, Mater. Charact. 143 (2018) 163-170, 10.1016/j.matchar.2018.04.009

[11] J.K. Algardh, T. Horn, H. West, Thickness dependency of mechanical properties for thin-walled titanium parts manufactured by Electron Beam Melting (EBM)®, Addit. Manuf. 12 (2016) 45-50, https://doi.org/10.1016/j.addma.2016.06.009

[12] N. Béraud, F. Vignat, F. Villeneuve, Improving dimensional accuracy in EBM using beam characterization and trajectory optimization, Addit. Manuf. 14 (2017) 1-6, https://doi.org/10.1016/j.addma.2016.12.002

[13] M.A. Lodes, R. Guschlbauer, C. Korner, Process development for the manufacturing of 99.94% pure copper via selective electron beam melting, Mater. Lett. 143 (2015) 298-301, 10.1016/j.matlet.2014.12.105

[14] A. Thomas, G. Fribourg, J.-J. Blandin, Effect of the build orientation on mechanical and electrical properties of pure Cu fabricated by E-PBF, Addit. Manuf. 48 (2021) 102393, https://doi.org/10.1016/j.addma.2021.102393

[15] L. Constantin, Z. Wu, N. Li, Laser 3D printing of complex copper structures, Addit. Manuf. 35 (2020) 101268, https://doi.org/10.1016/j.addma.2020.101268

[16] Green Light for New 3D Printing Process - Fraunhofer ILT. https://www.ilt.fraunhofer.de/en/press/press-releases/press-release-2017/press-release-2017-08-30.html.

[17] S.D. Jadhav, S. Dadbakhsh, L. Goossens, Influence of selective laser melting process parameters on texture evolution in pure copper, J. Mater. Process. Technol. 270 (2019) 47-58, 10.1016/j.jmatprotec.2019.02.022

[18] S. Gruber, L. Stepien, E. López, Physical and Geometrical Properties of

Additively Manufactured Pure Copper Samples Using a Green Laser Source, Materials 14(13) (2021) 3642, 10.3390/ma14133642

[19] S.D. Jadhav, L.R. Goossens, Y. Kinds, Laser-based powder bed fusion additive manufacturing of pure copper, Addit. Manuf. 42 (2021) 101990, 10.1016/j.addma.2021.101990

[20] J.-P. Kruth, X. Wang, T. Laoui, Lasers and materials in selective laser sintering, Assem. Autom. (2003), 10.1108/01445150310698652

[21] X.C. Yan, C. Chang, D.D. Dong, Microstructure and mechanical properties of pure copper manufactured by selective laser melting, Mat Sci Eng a-Struct 789 (2020) 139615, 10.1016/j.msea.2020.139615

[22] T.-T. Ikeshoji, K. Nakamura, M. Yonehara, Selective laser melting of pure copper, Jom 70(3) (2018) 396-400, 10.1007/s11837-017-2695-x

[23] E. Hori, Y. Sato, T. Shibata, Development of SLM process using 200 W blue diode laser for pure copper additive manufacturing of high density structure, J. Laser Appl. 33(1) (2021) 012008, 10.2351/7.0000311

[24] L. Kaden, G. Matthäus, R. Ramm, Additive manufacturing of pure copper using ultrashort laser pulses, Laser 3D Manuf. VI, International Society for Optics and Photonics, 2019, p. 109090D, 10.1117/12.2507401

[25] World premiere at Formnext: green laser from TRUMPF prints copper and gold. https://www.trumpf.com/en_US/presse/global-press-releases/press-release-detail-page/Press/world-premiere-at-formnext-green-laser-from-trumpf-prints-copper-and-gold/.

[26] S. Qu, J. Ding, J. Fu, High-precision laser powder bed fusion processing of pure copper, Addit. Manuf. 48 (2021) 102417, https://doi.org/10.1016/j.addma.2021.102417

[27] J. Fu, S. Qu, J. Ding, Comparison of the microstructure, mechanical properties and distortion of stainless steel 316 L fabricated by micro and conventional laser powder bed fusion, Addit. Manuf. 44 (2021) 102067, 10.1016/j.addma.2021.102067

[28] M. Khan, P.J.R.P.J. Dickens, Selective laser melting (SLM) of gold (Au), Rapid Prototyp. J. (2012), 10.1108/13552541211193520

[29] L. Lu, Y. Shen, X. Chen, Ultrahigh Strength and High Electrical Conductivity in Copper, Science 304(5669) (2004) 422-426, 10.1126/science.1092905

[30] P. Li, Y. Kim, A.C. Bobel, Microstructural origin of the anisotropic flow stress of laser powder bed fused AlSi10Mg, Acta Mater. 220 (2021) 117346, https://doi.org/10.1016/j.actamat.2021.117346

[31] O. Gokcekaya, T. Ishimoto, S. Hibino, Unique crystallographic texture formation in Inconel 718 by laser powder bed fusion and its effect on mechanical anisotropy, Acta Mater. 212 (2021) 116876, https://doi.org/10.1016/j.actamat.2021.116876

[32] K. Ujihara, Reflectivity of Metals at High Temperatures, J. Appl. Phys. 43(5) (1972) 2376-2383, 10.1063/1.1661506

[33] B. Vrancken, R.K. Ganeriwala, A.A. Martin, Microcrack mitigation during laser scanning of tungsten via preheating and alloying strategies, Addit. Manuf. 46 (2021) 102158, https://doi.org/10.1016/j.addma.2021.102158

[34] F. Bachmann, R. Hielscher, H. Schaeben, Grain detection from 2d and 3d EBSD data—Specification of the MTEX algorithm, Ultramicroscopy 111(12) (2011)

1720-1733

[35] M. Deutges, H.P. Barth, Y. Chen, Hydrogen diffusivities as a measure of relative dislocation densities in palladium and increase of the density by plastic deformation in the presence of dissolved hydrogen, Acta Mater. 82 (2015) 266-274, https://doi.org/10.1016/j.actamat.2014.09.013

[36] O. Andreau, I. Koutiri, P. Peyre, Texture control of 316L parts by modulation of the melt pool morphology in selective laser melting, J. Mater. Process. Technol. 264 (2019) 21-31, https://doi.org/10.1016/j.jmatprotec.2018.08.049

[37] N.T. Aboulkhair, I. Maskery, C. Tuck, On the formation of AlSi10Mg single tracks and layers in selective laser melting: Microstructure and nano-mechanical properties, J. Mater. Process. Technol. 230 (2016) 88-98, https://doi.org/10.1016/j.jmatprotec.2015.11.016

[38] L. Thijs, M.L. Montero Sistiaga, R. Wauthle, Strong morphological and crystallographic texture and resulting yield strength anisotropy in selective laser melted tantalum, Acta Mater. 61(12) (2013) 4657-4668, https://doi.org/10.1016/j.actamat.2013.04.036

[39] B. Soenen, A.K. De, S. Vandeputte, Competition between grain boundary segregation and Cottrell atmosphere formation during static strain aging in ultra low carbon bake hardening steels, Acta Mater. 52(12) (2004) 3483-3492, https://doi.org/10.1016/j.actamat.2004.03.046

[40] Y. Wang, D. Pan, Y. Zhao, Enhanced stability of retained austenites in quenched 25SiMn2MoV steel by electro-pulsing current, Mater. Sci. Eng., A 771 (2020) 138642, https://doi.org/10.1016/j.msea.2019.138642

[41] T. Voisin, J.-B. Forien, A. Perron, New insights on cellular structures strengthening mechanisms and thermal stability of an austenitic stainless steel fabricated by laser powder-bed-fusion, Acta Mater. 203 (2021) 116476, https://doi.org/10.1016/j.actamat.2020.11.018

[42] J.H. Hollomon, Tensile deformation, Aime Trans 12(4) (1945) 1-22

[43] M. Malý, D. Koutný, L. Pantělejev, Effect of high-temperature preheating on pure copper thick-walled samples processed by laser powder bed fusion, J. Manuf. Process. 73 (2022) 924-938

[44] Z. Li, Y. Cui, W. Yan, Enhanced strengthening and hardening via self-stabilized dislocation network in additively manufactured metals, Mater. Today  (2021), https://doi.org/10.1016/j.mattod.2021.06.002

[45] X. Yan, C. Chang, D. Dong, Microstructure and mechanical properties of pure copper manufactured by selective laser melting, Mater. Sci. Eng., A 789 (2020) 139615, https://doi.org/10.1016/j.msea.2020.139615

[46] J. Huang, X. Yan, C. Chang, Pure copper components fabricated by cold spray (CS) and selective laser melting (SLM) technology, Surf. Coat. Technol. 395 (2020) 125936, https://doi.org/10.1016/j.surfcoat.2020.125936

[47] H. Zhu, J. Chen, H. Chen, Loading Direction-Dependent Mechanical Properties of Columnar Polycrystal: A Molecular Dynamics Study, J. Mater. Eng. Perform. 30(3) (2021) 1970-1980, 10.1007/s11665-021-05480-2

[48] K. Ma, H. Wen, T. Hu, Mechanical behavior and strengthening mechanisms in

ultrafine grain precipitation-strengthened aluminum alloy, Acta Mater. 62 (2014) 141-155, https://doi.org/10.1016/j.actamat.2013.09.042

[49] J. Hou, W. Chen, Z. Chen, Microstructure, tensile properties and mechanical anisotropy of selective laser melted 304L stainless steel, J. Mater. Sci. Technol. 48 (2020) 63-71, https://doi.org/10.1016/j.jmst.2020.01.011

[50] A. Mehta, L. Zhou, H. Hyer, Microstructural characteristics and mechanical properties of additively manufactured Cu–10Sn alloys by laser powder bed fusion, Mater. Sci. Eng., A 838 (2022) 142775, https://doi.org/10.1016/j.msea.2022.142775

[51] Y.J. Yin, J.Q. Sun, J. Guo, Mechanism of high yield strength and yield ratio of 316 L stainless steel by additive manufacturing, Mater. Sci. Eng., A 744 (2019) 773-777, https://doi.org/10.1016/j.msea.2018.12.092

[52] Z. Zhang, J.-h. Zhang, J. Wang, Toward the development of Mg alloys with simultaneously improved strength and ductility by refining grain size via the deformation process, International Journal of Minerals, Metallurgy and Materials 28(1) (2021) 30-45, 10.1007/s12613-020-2190-1

[53] D. Gu, H. Chen, Selective laser melting of high strength and toughness stainless steel parts: The roles of laser hatch style and part placement strategy, Mater. Sci. Eng., A 725 (2018) 419-427, https://doi.org/10.1016/j.msea.2018.04.046

[54] W. Shifeng, L. Shuai, W. Qingsong, Effect of molten pool boundaries on the mechanical properties of selective laser melting parts, J. Mater. Process. Technol. 214(11) (2014) 2660-2667, https://doi.org/10.1016/j.jmatprotec.2014.06.002

[55] M. Shamsujjoha, S.R. Agnew, J.M. Fitz-Gerald, High Strength and Ductility of Additively Manufactured 316L Stainless Steel Explained, Metall. Mater. Trans. A 49(7) (2018) 3011-3027, 10.1007/s11661-018-4607-2

[56] C.X. Huang, K. Wang, S.D. Wu, Deformation twinning in polycrystalline copper at room temperature and low strain rate, Acta Mater. 54(3) (2006) 655-665, https://doi.org/10.1016/j.actamat.2005.10.002

[57] M.A. Meyers, O. Vöhringer, V.A. Lubarda, The onset of twinning in metals: a constitutive description, Acta Mater. 49(19) (2001) 4025-4039, https://doi.org/10.1016/S1359-6454(01)00300-7

[58] J.W. Christian, S. Mahajan, Deformation twinning, Prog. Mater. Sci. 39(1) (1995) 1-157, https://doi.org/10.1016/0079-6425(94)00007-7

[59] P. Sathiyamoorthi, J. Basu, S. Kashyap, Thermal stability and grain boundary strengthening in ultrafine-grained CoCrFeNi high entropy alloy composite, Mater. Des. 134 (2017) 426-433, https://doi.org/10.1016/j.matdes.2017.08.053

[60] J.P. Hou, R. Li, Q. Wang, Breaking the trade-off relation of strength and electrical conductivity in pure Al wire by controlling texture and grain boundary, J. Alloys Compd. 769 (2018) 96-109, https://doi.org/10.1016/j.jallcom.2018.07.358

[61] S. Riedel, J. Röber, T. Geßner, Electrical properties of copper films produced by MOCVD, Microelectron. Eng. 33(1) (1997) 165-172, https://doi.org/10.1016/S0167-9317(96)00042-1

[62] Y.K. Huang, A.A. Menovsky, F.R. de Boer, Electrical resistivity of nanocrystalline copper, Nanostructured Materials 2(5) (1993) 505-513, https://doi.org/10.1016/0965-9773(93)90168-B

[63] S.J. Raab, R. Guschlbauer, M.A. Lodes, Thermal and Electrical Conductivity of 99.9% Pure Copper Processed via Selective Electron Beam Melting Adv. Eng. Mater. 18(9) (2016) 1661-1666, 10.1002/adem.201600078

[64] J.C. Ledford. Development of Processing Techniques for the Fabrication of Pure Copper Components Utilizing EB-PBF, PhD Thesis, North Carolina State University, Ann Arbor, (2021)